Efficient electrooxidation of 5-hydroxymethylfurfural via phosphate intercalated hydroxides: A dual-cycle mechanism

Tianli Hui [a], Haowei Liu [a], Tonghui Li [a], Jinbo Pan [a,b], Tao Zheng [a,*], Rui Zhang [a], Xianghai Meng [a], Haiyan Liu [a], Zhichang Liu [a], Chunming Xu [a]

[a] State Key Laboratory of Heavy Oil Processing, China University of Petroleum, Beijing 102249, China
[b] Department of Chemistry, Johannes Gutenberg University Mainz, Mainz 55128, Germany

ARTICLE INFO

ABSTRACT

The electrooxidation of 5-hydroxymethylfurfural (HMF) has emerged as a promising way to generate high-value-added products. However, evoking high-valence state NiOOH species as active sites to realize high current density remains a challenge. Herein, we report an efficient electrocatalyst for HMF electrooxidation based on phosphate anion intercalated layered double hydroxides (NiCo-Pi-LDHs). Onset potential at 1.16 V vs. RHE and current density of 200 mA/cm^2 at 1.41 V vs. RHE were realized. The intercalated phosphates act as proton transfer intermediates, facilitating the dehydrogenation of hydroxides to form oxyhydroxides while the protonated phosphate generated. The obtained oxyhydroxide oxidized HMF to 2,5-furandicarboxylic (FDCA) while cycling backward to hydroxide, accompanied by the cycle of protonated phosphate to phosphate. This novel strategy with dual-cycle of phosphate and nickel species can effectively evoke NiOOH species, thereby speeding up the reaction rate and having a great potential for biomass upgrading.

1. Introduction

The chemical utilization of biomass resources has attracted much more attention because it makes outstanding contributions to carbon neutrality [1–5]. Being a significant biomass-derived platform chemical, 5-hydroxymethylfurfural (HMF) can be used to produce a variety of high-value-added products. Particularly, 2,5-furandicarboxylic acid (FDCA) generated via HMF oxidation acts as an essential building block for biomass-based polymers with remarkable economic value [6,7]. Selective oxidation of HMF has been conventionally conducted by thermocatalysis, which requires noble metal catalysts and harsh reaction conditions to achieve high yields, raising economic and carbon emission worries [8,9]. Compared to that, electrocatalytic oxidation with a lower carbon footprint can be used to produce FDCA from HMF without noble metal catalysts or intensive energy input. More delightfully, the combination of anodic HMF oxidation reaction (HMFOR) and cathodic hydrogen evolution reaction (HER) can realize the co-production of value-added chemicals and green hydrogen, not only reducing the energy consumption but also increasing the economic benefit of water electrolyzer [10,11]. Therefore, the exploitation of efficient electrocatalysts for electrochemical HMFOR processes becomes more economical and feasible.

Non-noble metal electrocatalysts for HMFOR, which exhibit relatively high catalytic activity and superior FDCA selectivity, have been extensively developed. However, realizing industrial current density (> 200 mA/cm^2) of HMFOR without inducing competitive oxygen evolution reaction (OER) is still a great challenge [12,13]. This is because the current density of HMFOR does not simply increase gradually with the increasing voltage due to the competition with OER at high potentials [14]. Thus, in order to enhance the activity at limited potential intervals, research interest focused on how to create efficient active sites and increase their amount. Due to their good inherent oxygen affinity and fast reaction kinetics, nickel-based materials were widely investigated [15]. Previous work revealed the important role of Ni^{3+} species, which were able to catalyze HMFOR without triggering OER [16–18]. Therefore, the generation of Ni^{3+} species was regarded as the core of HMFOR electrocatalysts design. Extensive work demonstrated that suitable metal doping boosted partial charge transfer and evoked Ni^{3+} species NiOOH, thereby accelerating HMF oxidation reaction rate [19,20]. Especially, the synthesized layered double hydroxides (LDHs) materials were more favorable for improving the dispersion of nickel atoms and thus increasing the number of Ni^{3+} sites [21,22]. More importantly, Du and

---

co-workers revealed the dynamic transformation between $Ni(OH)_2$ and NiOOH during HMFOR [23]. To be specific, they proposed that NiOOH chemically oxidized HMF to generate FDCA, and itself was rapidly reduced backward to $Ni(OH)_2$. The applied anodic potential subsequently drove the transformation of $Ni(OH)_2$ into NiOOH to circulate the HMF oxidization process. In conclusion, HMF electrooxidation is highly dependent on the generation of Ni^{3+} sites, and thus promoting the cycle of $Ni(OH)_2$-NiOOH transformation plays a key role in catalytic activity enhancement.

In order to promote the cycle of nickel species, attention needs to be paid to the dehydrogenation process of nickel hydroxides fundamentally. From $Ni(OH)_2$ to NiOOH, one hydrogen atom needs to be removed from per formula unit. In the case of multilayer $Ni(OH)_2$, the hydrogen atoms need to diffuse from the interior region to the surface or edge before participation in the dehydrogenation process, which is limited by diffuse barriers [24]. Thus, optimizing the dehydrogenation step in hydroxides interlamellar space becomes a key point to accelerate NiOOH formation. Furthermore, the dehydrogenation occurring in the interlamellar space of hydroxides contributes to the generation of NiOOH species in the bulk phase, which is often the limiting step for most organic electrooxidations [25]. Therefore, improving the interlayer dehydrogenation process becomes especially important. Notably, during the oxygen evolution reaction, Grimaud's group found that the phosphate anion on the perovskite surface acted as a proton transfer intermedia, which could facilitate the dehydrogenation process [26]. Different from proton receptor actions, the strong nucleophilic phosphate anions underwent both protonation and dehydrogenation during this process, in which a protonation circle was formed. Inspired by the promotion of phosphate ion (Pi) on the dehydrogenation process, we intend to introduce phosphate groups as guest anions in the interlayer of layered double hydroxides. The intercalated phosphate is expected to enhance the dehydrogenation of hydroxides as a proton transfer intermediate and to further evoke high-valence nickel species. Thus, the introduction of the phosphate protonation circle is anticipated to accelerate the $Ni(OH)_2$/NiOOH transformation circle and to promote HMFOR catalytic performance.

In this work, we fabricated intercalated NiCo-Pi-LDHs catalysts by introducing phosphate ions into the interlayer of NiCo-LDHs via hydrothermal and anion exchange method. The synthesized catalyst nanosheets were uniformly coated on nickel foam surface, serving as NiCo-Pi-LDHs/NF electrodes for electrooxidation of HMF to FDCA. The XRD, FTIR characterization, and DFT calculation results clearly confirmed the successful intercalation of phosphate ions in NiCo-Pi-LDHs. Over the catalysts, onset potential at 1.16 V vs. RHE and 200 mA/cm^2 current density at 1.41 V vs. RHE were realized, which were comparable to those over the state-of-the-art catalysts. In addition, a novel dual-cycle mechanism was proposed, which can provide a feasible approach to accelerate hydroxide/oxyhydroxide dynamic transformation and evoke high valence state of Ni for HMFOR, and also draws some references to other organic molecule electrooxidation reactions.

2. Experimental details

2.1. Chemical materials

Nickel acetylacetonate (95 %), cobalt acetylacetonate (97 %), triethanolamine (98 %), sodium phosphate (96 %), potassium hydroxide (99.99 %), 5-hydroxymethylfurfural (95 %), 5-hydroxymethyl-2-furancarboxylic acid (99 %), 5-formyl-furancarboxylic acid (99 %), 2,5-dihydroxymethylfuran (99 %) and 2,5-furandicarboxylic acid (99 %) were purchased from Aladdin Bio-Chem Technology Co. Ltd (Shanghai, China). Ethanol (95 %) and sodium carbonate (99.8 %) were purchased from Innochem Chemical Reagent Co. Ltd (Beijing, China). Hydrochloric acid (37 % solution in water) was purchased from Beijing Tongguang Fine Chemical Co. Ltd (Beijing, China). Nickel foam (NF) was purchased

from Shengernuo Technology Company (Suzhou, China). Deionized water (18.25 MΩ·cm) was obtained from Ulupure purification system. The deionized water for catalyst preparation was boiled to remove dissolved carbon dioxide before use.

2.2. Fabrication of NiCo-LDHs precursor on NF substrates

NF pieces were ultrasonically pretreated for 15 min with an aqueous solution (1.0 M HCl), ethanol, and deionized water, respectively. Then, the obtained NF pieces were rinsed with deionized water and finally dried in a vacuum oven for further use. The fabrication of NiCo-LDHs precursor was carried out by hydrothermal method. Nickel acetylacetonate (225 μmol), cobalt acetylacetonate (75 μmol), and triethanolamine (1.275 mmol) were added into a mixed solvent containing 7.5 mL deionized water and 7.5 mL ethanol to form a homogeneous solution, and then transferred to a stainless-steel autoclave with a piece of pretreated nickel foam. For the synthesis of $Ni(OH)_2$/NF and a series of NiCo-Pi-LDHs/NF with different Ni/Co ratios, the total number of moles of metal salts was kept constant at 300 μmol. The autoclave was placed in a 120 °C oven for 6 h and then cooled to room temperature. The obtained NiCo-LDHs/NF was rinsed with deionized water and ethanol until pH=7. Powders were also collected from the remaining solution and rinsed until pH=7. A vacuum dryer was used to dry the samples for at least 6 h.

2.3. Conversion of NiCo-LDHs/NF into NiCo-Pi-LDHs/NF and NiCo-Ci-LDHs/NF

The obtained NiCo-LDHs/NF precursor was converted into intercalated NiCo-LDHs/NF by anion exchange. In a typical process, the NiCo-LDHs/NF was immersed in an electrolyte containing 1 M KOH and 0.1 M Na_3PO_4 for 24 h. For comparison, the NiCo-LDHs/NF was also immersed into 1 M KOH and 0.1 M Na_2CO_3 for 24 h and the obtained electrode denoted as NiCo-Ci-LDHs/NF. Besides, the powder samples were also collected and further grinded for characterization. The catalyst powders used for XPS and EDS analysis were exfoliated from nickel foam substrates by continuous shaking on a shaker.

2.4. Characterization methods

X-Ray diffraction (XRD) characterization was performed by an Empyrean X-Ray powder diffractometer (PANalytical, Netherland) using a Cu Kα radiation with a scan speed of 5°/min in the range of 2θ=5–90°. The fourier transform infrared spectroscopy (FTIR) was recorded by using a Tensor II instrument (Bruker, Germany). X-ray photoelectron spectroscopy (XPS) was performed on a K-Alpha photoelectron spectrometer (Thermo Fisher, USA) with Al Kα radiation (spot size =300 μm). For all catalysts, the calibration peak was the C 1 s peak at 284.6 eV. Field emission scanning electron microscope (FESEM) with energy-dispersive X-ray spectroscopy (EDX) spectrometer was conducted by Quanta 200 F (FEI, Netherland) to observe the microscope morphology and analyze the elements distribution. Transmission electron microscopy (TEM) images were obtained by a F20 microscope (FEI, USA) at 200 kV. Inductively coupled plasma optical emission spectrometer (ICP-OES) was carried out on a ICPE-9800 (Shimadzu, Japan). The texture properties of the samples were measured by a BSD-660 M specific surface area and pore size analyzer (BSD Instrument, China). The total specific surface area and pore distribution were calculated by Brunauer-Emmett-Teller (BET) method and Barrett-Joyner-Halenda (BJH) method, respectively.

2.5. Electrochemical measurements

Electrochemical measurements were performed on an Interface 1010E electrochemical workstation (Gamry, USA) with a three-electrode configuration. The as-prepared electrodes were used as the

working electrode, Pt sheet as the counter electrode, and Hg/HgO as the reference electrode. All the potentials reported were converted into reversible hydrogen electrode (RHE). The calibration of the reference electrode was performed in electrolyte with a commercial RHE from Gaskatel HydroFlex (Germany). 1.0 M aqueous KOH with or without the presence of 50 mM HMF was used as the electrolyte. Linear sweep voltammetry (LSV) curves were collected at a scan rate of 5 mV/s with 90 % iR compensation. The electrochemically active surface area (ECSA) was estimated by calculating the electrochemical double layer capacitances (C_{dl}) in a non-Faradaic potential region. Cyclic voltammetry (CV) was performed from 0.95 V to 1.05 V vs RHE with scan rates of 20, 40, 60, 80, and 100 mV/s. ECSA=C_{dl}/C_S, where C_S represents the C_{dl} of ideally flat electrode taken as 0.04 mF/cm^2 for electrolyte. Electrochemical impedance spectroscopy (EIS) was carried out over a frequency range from 10^5 to 10^{-1} Hz. Long-term OER electrolysis test was carried out at potential of 1.6 V vs. RHE in 1.0 M KOH for 10 h. The HMF oxidation tests were performed in an H-type cell configuration. FAA-3-PK-130 (Fumasep, Germany) was used as anion exchange membrane.

2.6. Products quantification

The HMF and oxidation products were analyzed by a high-performance liquid chromatography (HPLC, ThermoFisher Vanquish, Germany) with an ultraviolet-visible detector set at 260 nm. Sulfuric acid (H_2SO_4, 0.01 M) was used as the mobile phase with a constant flow rate of 0.8 mL/min and a column temperature of 60 °C. The electrolyte solution (20 μL) was diluted to 4.0 mL with dilute sulfuric acid solution to make the pH below 7.0, and then 20 μL of the diluted solution was injected directly into a Bio-Rad HPX-87 H column. The identification of the HMF and its various oxidation products was achieved by retention times in the chromatograms with those of the standard solution, and their concentrations were determined from calibration curves.

The conversion of HMF, the selectivity of FDCA, and the faradaic efficiency (FE) were calculated according to the equations below, respectively.

HMF conversion(%) = $\frac{\text{mol of consumed}}{\text{mol of HMF initial}} \times 100\%$

FDCA selectivity(%) = $\frac{\text{mol of FDCA formed}}{\text{mol of HMF consumed}} \times 100\%$

FE(%) = $\frac{\text{mol of FDCA formed}}{(\text{charge}/(6 \times F))} \times 100\%$

The F represented the Faraday constant (96485 C/mol).

2.7. Calculation methods

Density functional theory (DFT) simulations were implemented using Vienna ab initio simulation package. The Generalized Gradient Approximation (GGA) of Perdew-Burke-Ernzerh (PBE) was employed to describe the exchange an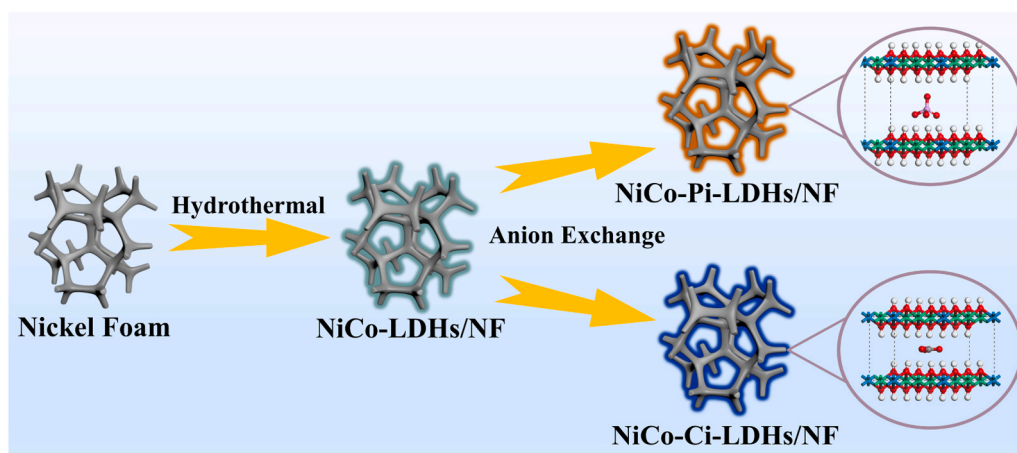d correlation energy density function. The initial structural models of intercalated NiCo-LDHs were constructed based on standard diffraction data (PDF#40–216) and relevant literature [27]. In the calculation, a 5×5×5 Monkhorst-Pack type of K-point sampling was used in Brillouin zone integrations for the bulk. The intercalated NiCo-LDHs structures were optimized by using 450 eV as the cutoff energy. The change criterion of all energies was set to 10^{-4} eV and the maximum force was 0.05 eV/Å. DFT+U method was used to describe correlation for 3d metals with U_{Ni}= 4.0 and U_{Co}= 3.8.

3. Results and discussion

3.1. Structure and morphological characterization

The synthesis process of the intercalated NiCo-LDHs/NF was illustrated in Scheme 1. First, the NiCo-LDHs/NF precursor was obtained via hydrothermal method, similar to previous reports [28,29]. The NiCo-LDHs powder was collected and characterized by X-ray diffraction. As shown in Figure S1, the sample exhibited the typical basal reflections of layered double hydroxides, suggesting the successful synthesis of NiCo-LDHs materials. Due to the avoidance of carbonate introduction during the synthesis process, the peak of the (003) plane located at 2θ=11.4° was ascribed to the intercalation of OH⁻ [30]. According to the sequence of anion exchange in LDHs (PO_4^{3-} >CO_3^{2-} >OH⁻), the OH⁻ intercalated NiCo-LDHs precursor could be converted into phosphate or carbonate intercalated NiCo-LDHs [31]. NiCo-Pi-LDHs and NiCo-Ci-LDHs were obtained by immersing the NiCo-LDHs precursor with electrolyte containing phosphate or carbonate for 24 h, to ensure the sufficient intercalation of desirable anion. To characterize the intercalation structure, the powder samples of NiCo-Pi-LDHs and NiCo-Ci-LDHs were also collected and their XRD patterns and FTIR spectra were shown in Fig. 1.

As depicted in Fig. 1A, the XRD patterns of synthesized samples both exhibited the typical characteristic diffractions of NiCo-LDHs materials (JCPDS No. 40–216), including (003), (006), (012), and (110) facets, which suggested that synthesized NiCo-LDHs materials were well-structured. It was worth noting that the pattern of NiCo-Pi-LDHs exhibited a lower diffraction angle of (003) crystal facet than that of NiCo-Ci-LDHs, which was attributed to the variation of interlayer spacing. The basal spacing calculated by the Bragg formula showed that in NiCo-Ci-LDHs, the (003) diffraction peak occurred at 2θ=11.6°, corresponding to a basal spacing of 7.6 Å. While for NiCo-Pi-LDHs, the (003) diffraction peak occurred at 2θ=8.9°, with a corresponding basal space of 9.9 Å, much larger than that of carbonate intercalation. This regular variation in basal space was consistent with the size ordering of phosphate and carbonate, proving the intercalation of phosphate and carbonate [32]. DFT calculations were also employed to further confirm

Scheme 1. Synthesis process for NiCo-Pi-LDHs/NF and NiCo-Ci-LDHs/NF by hydrothermal and anion exchange method.
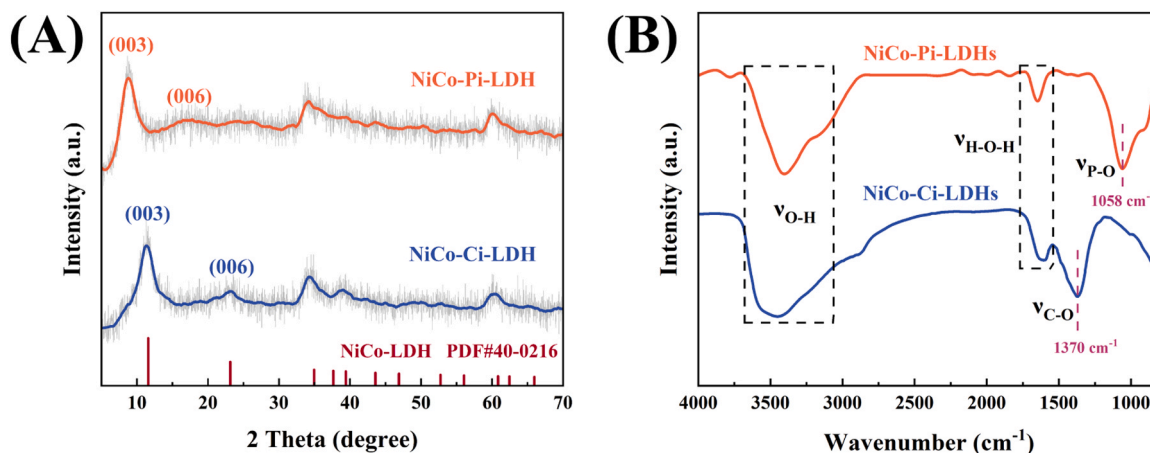
Fig. 1. (A) XRD patterns and (B) FTIR spectra of NiCo-Pi-LDHs and NiCo-Ci-LDHs powder.

the disparity of interlayer spacing (Figure S2 and Table S1). As shown in Table S1, the theoretical interlayer distances were 9.8 Å for NiCo-Pi-LDHs and 7.6 Å for NiCo-Ci-LDHs, which were in good agreement with the experimental data.

To verify the intercalated anion, FTIR measurement was conducted. As shown in Fig. 1B, the H-O-H bending and the O-H symmetric vibrational bands of metal hydroxide layers appeared in 1610–1630 cm^{-1} and 3405–3450 cm^{-1}, respectively. Obviously, the spectrum of NiCo-Pi-LDHs exhibited an intense band appearing at 1058 cm^{-1} corresponding to the P-O stretching vibration of phosphate ion, indicating the successful intercalation of phosphate anion in NiCo-LDHs [33]. The band at 1370 cm^{-1} was associated with the stretching vibration of the carbonate group in FTIR spectrum of NiCo-Ci-LDHs [34]. In general, LDHs materials readily capture carbon dioxide from the atmosphere, resulting in carbonates occupying the interlayer space of LDHs [35,36]. However, it should be noted that no significant vibration band related to CO$_3^{2-}$ was observed in NiCo-Pi-LDHs, proving that the interaction between the phosphate anion and host layer was stronger compared to the carbonate anion. The relative binding energies between the NiCo-LDHs matrix and the intercalated anions were calculated by DFT and listed in Table S2. The relative binding energy of NiCo-Pi-LDHs (-5.20 eV) was much larger than that of NiCo-Ci-LDHs (-4.53 eV), confirming the stronger interaction of phosphate anions with laminates [30,37]. These results further suggested that phosphate anions have better stability in NiCo-LDHs interlayer space, which might contribute to the improvement of catalytic stability. Combining XRD, FTIR, and DFT calculation, the above results convincingly verified the formation of a series of NiCo-LDHs materials and the presence of the intercalated anions in the interlayer space. Notably, phosphate anions exhibited a stronger binding capacity than carbonate anion in the interlayer space, indicating outstanding

structural stability.

To investigate the morphology and structural features of catalysts, FESEM was conducted on the bare nickel foam, NiCo-Pi-LDHs/NF and NiCo-Ci-LDHs/NF electrodes. As shown in Figure S3, the bare nickel foam showed a zigzag hollow structure with a smooth surface, whereas the nickel foam surface of NiCo-Pi-LDHs/NF was covered by a thin layer and thus became rough. The element distribution on the nickel foam substrate, as shown in Figure S4, showed that the corresponding elements were homogeneously distributed on the nickel foam surface for NiCo-Pi-LDHs/NF and NiCo-Ci-LDHs/NF, indicating a favorable distribution of the deposited NiCo-LDHs. Fig. 2A further showed the microscopic morphology of NiCo-Pi-LDHs/NF electrode, where NiCo-Pi-LDHs nanosheets were vertically aligned on nickel foam. Such two-dimensional nanosheets formed on nickel foam constructed ordered array structures, significantly increasing the surface area and promising more active sites [38–40]. As shown in Figure S5A, NiCo-Ci-LDHs/NF exhibited the similar morphological characteristics and were not significantly different from NiCo-Pi-LDHs/NF. In order to quantify the elemental composition of LDH nanosheets, NiCo-LDHs powders were also characterized. EDX element mapping images displayed in Fig. 2B and Figure S5B revealed the presence and the homogeneous distribution of Ni, Co, P or C, and O elements throughout NiCo-Pi-LDHs and NiCo-Ci-LDHs. It should be emphasized that in contrast to NiCo-Ci-LDHs, the C element abundance in NiCo-Pi-LDHs was obviously lower, attributed to the intercalation of phosphate. The element contents measured by EDX spectra were listed in Table S3, revealing the similar Ni/Co ratio of NiCo-Pi-LDHs and NiCo-Ci-LDHs. ICP-OES was conducted to obtain precise elemental content analysis results. As shown in Table 1, the content of phosphorous in NiCo-Pi-LDHs reached 16.3 wt%, providing sufficient phosphate anions for intercalation structure. In
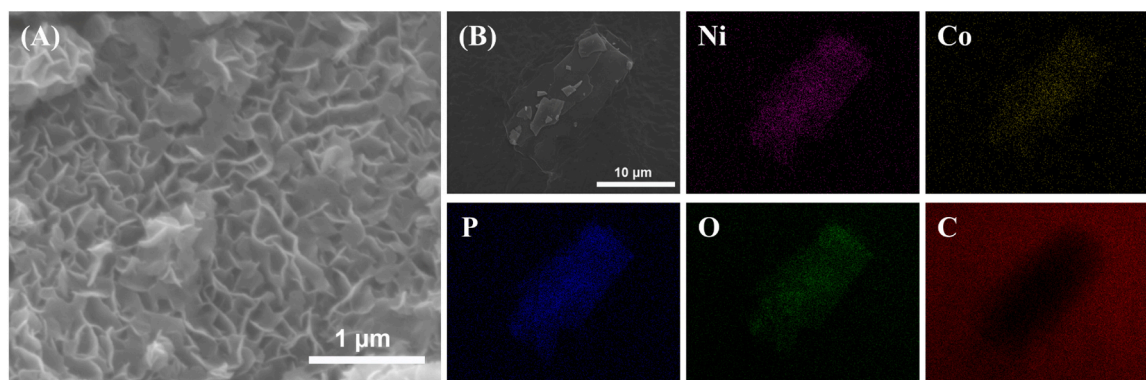

Fig. 2. (A) FESEM image of NiCo-Pi-LDHs/NF and (B) EDX mapping images of NiCo-Pi-LDHs powder.

Table 1

The element contents analysis of NiCo-Pi-LDHs and NiCo-Ci-LDHs powder measured by ICP-OES.

Sample	Ni (wt%)	Co (wt%)	P (wt%)	Ni/Co (at%)
NiCo-Pi-LDHs	26.0	8.3	16.3	3.1
NiCo-Ci-LDHs	32.1	11.0	-	2.9

addition, NiCo-Pi-LDHs and NiCo-Ci-LDHs exhibited similar Ni/Co atomic ratios of 3.1 and 2.9, respectively, indicating that the anion exchange step had no obvious impact on the Ni/Co ratio. The nanostructural morphology and structure of NiCo-Pi-LDHs were further analyzed by TEM. Figure S6A displayed NiCo-Pi-LDHs nanosheets with dimensions in hundreds of nanometers, which was consistent with the observations made by SEM. The HRTEM image (Figure S6B) displayed a lattice distance of ~0.26 nm, corresponding to the (012) crystal plane of NiCo-LDHs phase [41]. More information regarding the structure of the samples were detected by the N_2 adsorption-desorption test. As displayed in Table S4, similar specific surface area determined from the BET method and same average pore size measured from the BJH method were obtained for two samples (NiCo-Pi-LDHs: 11.8 m^2/g, 3.9 nm; NiCo-Ci-LDHs: 11.2 m^2/g, 3.9 nm). Therefore, the surface area and pore structure can be excluded for the possible contributions to the catalytic performance discrepancy of NiCo-Pi-LDHs and NiCo-Ci-LDHs. As shown in Figure S7, both samples showed similar adsorption-desorption profiles, in which the obvious hysteresis loops suggested their mesoporous character. Relevant research revealed that the mesoporous structure can be beneficial for the alleviation of diffusional limitations of reactants and products within the channels [42,43]. The above results strongly manifested the successful introduction of phosphate anion in NiCo-Pi-LDHs/NF. Meanwhile, the NiCo-Pi-LDHs nanosheets aligned on zigzag nickel foam to form a thin coating layer, which is favorable for electrical conductivity and mass transfer [44,45].

3.2. Electrochemical measurement for HMFOR

The HMFOR and OER performance of NiCo-Pi-LDHs/NF and NiCo-Ci-LDHs/NF were evaluated in a standard three electrodes system. LSV curves were collected in 1.0 KOH aqueous solution with and without 50 mM HMF, respectively. As shown in Fig. 3A, NiCo-Pi-LDHs/NF required an onset potential at ~ 1.48 V vs. RHE for OER, lower than that of NiCo-Ci-LDHs/NF (1.53 V vs. RHE). The anodic peaks located at ~1.30 V vs. RHE were attributed to the electrochemical oxidation of Ni^{2+}, leading to the formation of oxidation species NiOOH, which could serve as the active sites for HMFOR [16]. It should be noted that the anodic peak of NiCo-Pi-LDHs/NF was much higher than that of NiCo-Ci-LDHs/NF. This implied that the intercalation of phosphate enhanced the surface reconstruction and therefore induced more high-valence nickel sites. Upon adding 50 mM HMF, a dramatic shift of onset potential to 1.16 V vs. RHE was observed, demonstrating that HMFOR on NiCo-Pi-LDHs/NF electrode was thermodynamically more favorable than OER. More importantly, the current density increased sharply at ~1.27 V vs. RHE, which was consistent with the potential of the Ni^{2+} oxidation peak. This well indicated that the high-valence state Ni^{3+} species was the dominant active site for HMFOR. For NiCo-Ci-LDHs/NF, the potential to reach high current densities were much higher than NiCo-Pi-LDHs/NF. As depicted in Fig. 3B, the HMFOR potentials for achieving current densities of 10, 50, and 100 mA/cm^2 by NiCo-Pi-LDHs/NF were 1.23, 1.29, and 1.32 V vs. RHE, respectively, appreciably lower than those by NiCo-Ci-LDHs/NF (1.25, 1.37 and 1.50 V vs. RHE). For NiCo-Pi-LDHs/NF, the potential to reach 200 mA/cm^2 was only 1.41 V vs. RHE for HMFOR, which was competitive with the literatures [21,46–53]. As shown in Fig. 3C and Table S5, NiCo-Pi-LDHs catalyst exhibited higher current density than most previously reported catalysts, similar to the state-of-the-art nickel sulfides catalysts.

To verify the role of phosphate intercalation, the HMFOR and OER performance of $Ni(OH)_2$-Pi/NF and $Ni(OH)_2$-Ci/NF were also
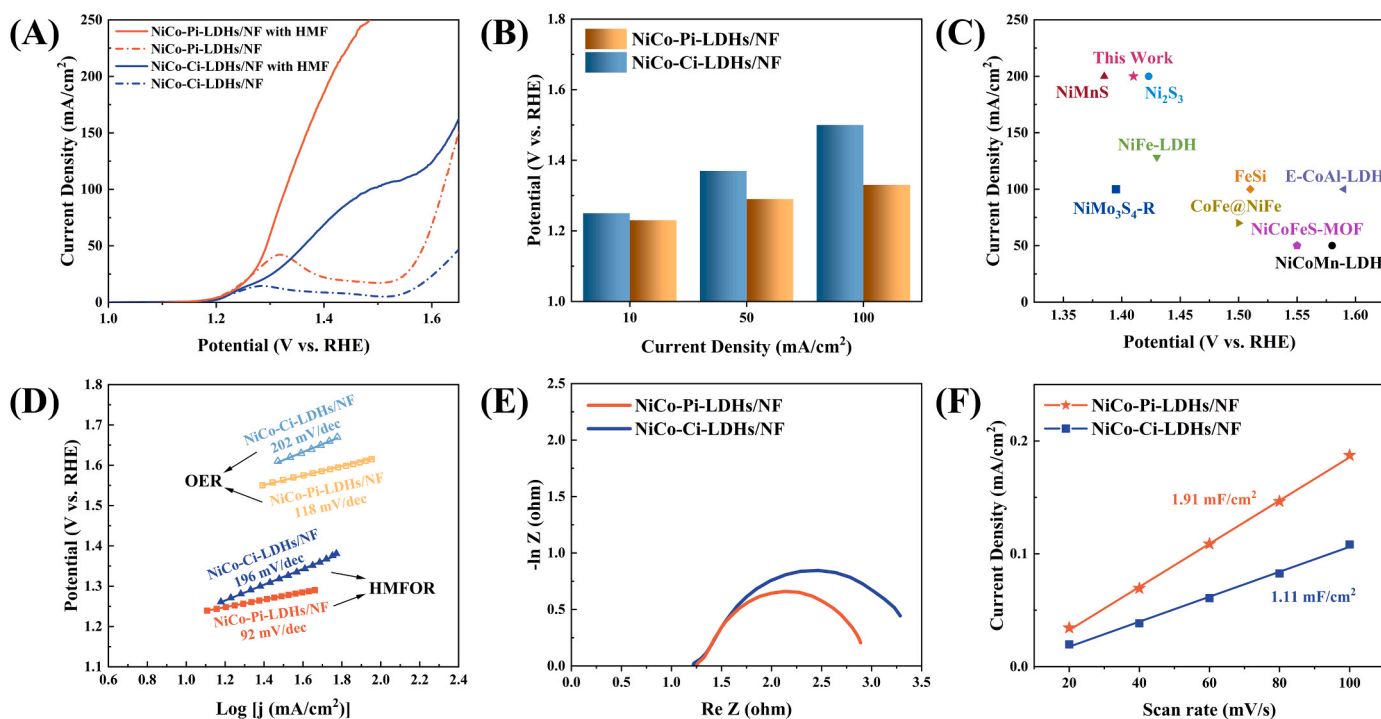

Fig. 3. (A) LSV curves of NiCo-Pi-LDHs/NF and NiCo-Ci-LDHs/NF in 1.0 M KOH solution with (solid lines) and without (dot-dash lines) 50 mM HMF. (B) Potential required for delivering different current densities using the NiCo-Pi-LDHs/NF and NiCo-Ci-LDHs/NF in 1.0 M KOH solution with 50 mM HMF. (C) Performance comparison of NiCo-Pi-LDHs catalyst with those previously reported electrocatalysts. (D) Tafel plots of NiCo-Pi-LDHs/NF and NiCo-Ci-LDHs/NF. (E) Nyquist plots of NiCo-Pi-LDHs/NF and NiCo-Ci-LDHs/NF. (F) Capacitive current densities for HMFOR under various scan rates of NiCo-Pi-LDHs/NF and NiCo-Ci-LDHs/NF.

investigated, and the results are shown in Figure S8. Similar to NiCo-Pi-LDHs, the intercalation of phosphate in Ni(OH)$_2$ also enhanced the anodic peak associated with Ni^{2+} oxidation. More importantly, the potential of Ni(OH)$_2$-Pi/NF to reach 200 mA/cm^2 was 1.52 V vs. RHE, while the Ni(OH)$_2$-Ci/NF only exhibited 104 mA/cm^2 at the same potential. This result strongly manifested that the intercalation of phosphate induced more high-valence nickel sites to realize the higher current density. Moreover, the NiCo-Pi-LDHs with different P contents were also synthesized and evaluated. As shown in Figure S9A, the P content gradually increased with the extension of the anion exchange time, reaching 8.6 wt%, 14.2 wt%, and 16.3 wt% at 8 h, 16 h, and 24 h, respectively. When the anion exchange time was further extended to 32 h, the P content was essentially unchanged (16.5 wt%), indicating that the phosphate anion was saturated in interlayer space. As displayed in Figure S9B, NiCo-Pi-LDHs/NF with different anion exchange time exhibited similar onset potentials around ~1.16 V vs. RHE. More importantly, with increasing phosphorus content, the current density of NiCo-Pi-LDHs/NF at 1.40 V significantly increased from 86 mA/cm^2 to 134 mA/cm^2 and 186 mA/cm^2. As a comparison, the current density of NiCo-Ci-LDHs/NF at the same potential was only 69 mA/cm^2. This positive correlation between current density and P content well demonstrated that the intercalated phosphate was able to induce more high-valence nickel sites to promote catalytic activity.

Another important issue is the effect of Ni/Co atomic ratio on catalytic performance. In the absence of Co, the onset potential of Ni(OH)$_2$-Pi/NF was 1.28 V vs. RHE, which was consistent with the oxidation of Ni^{2+}. Compared to NiCo-Pi-LDHs/NF, the much higher onset potential of Ni(OH)$_2$-Pi/NF suggested that Co was effective in reducing HMFOR onset potential. It was ascribed to the electronic interaction between Ni and Co, which reduced the oxidation potential required to generate high valence metal cations [54]. NiCo-Pi-LDHs/NF electrodes with different Ni/Co ratios were also synthesized and their HMFOR performances were evaluated. Figure S10 showed that for NiCo-Pi-LDHs/NF with varying Ni/Co ratios, the potentials required to reach 10 mA/cm^2 all decreased compared to Ni(OH)$_2$-Pi/NF (1.34 V vs. RHE), suggesting that the introduction of Co can modulate the electronic structure of catalysts and reduce the reaction potential. However, the excessive doping of Co resulted in a decrease in activity. Current densities at 1.40 V vs. RHE for NiCo-Pi-LDHs/NF with Ni/Co ratios of 5:1, 4:1, and 3:1 were 121, 141, and 186 mA/cm^2, respectively, higher than that of Ni(OH)$_2$-Pi/NF (106 mA/cm^2). For the Ni/Co ratios of 2:1 and 1:1, excessive Co doping led to a significant reduction in the number of Ni sites, which reduced the current densities to 60 and 51 mA/cm^2, respectively. It suggested that excessive Co was not beneficial in enhancing catalytic activity, further clarifying that Ni was the dominant active site for HMFOR. More importantly, since Ni was the dominant active site in HMFOR, the intercalation of phosphate at an appropriate Ni/Co ratio contributed to the generation of high-valence Ni sites and thus improved catalytic activity. The above results indicated that Co reduced the reaction potential, while intercalated phosphate induced high-valence nickel species to enhance the current density, and they synergistically improved the HMFOR activity.

The intercalation of phosphate anion also exerted an influence on the electrooxidation kinetics. As depicted in Fig. 3D, the Tafel slopes of NiCo-Pi-LDHs/NF and NiCo-Ci-LDHs/NF were calculated to be 118 mV/dec and 202 mV/dec for OER, 92 mV/dec and 196 mV/dec for HMFOR, respectively. For both anodic reactions, the Tafel slopes decreased as a result of phosphate anion intercalation, demonstrating the higher electron transfer rates of phosphate intercalating. Additionally, the Tafel slopes of HMFOR were lower than those of OER for both catalysts. This clearly indicated that the interfacial charge transfers between the HMF molecule and the catalysts was more readily achieved. The Nyquist plot of NiCo-Pi-LDHs/NF (Fig. 3E) exhibited a smaller semicircle than that of NiCo-Ci-LDHs/NF, further confirming that a faster charge transfer was attained on the surface.

In order to gain insight into the intrinsic activities of NiCo-Pi-LDHs/

NF and NiCo-Ci-LDHs/NF, the electrochemical surface areas (ECSA) in HMFOR were compared by estimating the electrochemical double-layer capacitance (C$_{dl}$) in the non-faradaic regions (Figure S11). As shown in Fig. 3F, the C$_{dl}$ values of NiCo-Pi-LDHs/NF and NiCo-Ci-LDHs/NF were calculated to be 1.91 mF/cm^2 and 1.11 mF/cm^2, respectively. It clearly revealed that the intercalation of phosphate anion resulted in an increase of C$_{dl}$ value as well as ECSA. In addition, to demonstrate the influence of phosphate intercalation on the intrinsic activity, the ECSA-normalized current density was calculated as shown in Figure S12. At the potential of 1.4 V vs. RHE, NiCo-Pi-LDHs/NF showed higher intrinsic activity of HMFOR, being 1.7 times as high as that of NiCo-Ci-LDHs/NF. The above results verified that the intercalation of phosphate anion contributed to the exposition of more active sites and the promotion of intrinsic activity.

3.3. Evaluation of HMFOR products

Fig. 4A shows the two possible pathways for HMFOR. The aldehyde group or hydroxyl group on the Furan ring can be selectively oxidized to generate 5-hydroxymethyl-2-furancarboxylic acid (HMFCA) or 2,5-furandicarboxaldehyde (DFF), respectively. These two intermediates are further oxidized to 5-Formylfuran-2-carboxylic acid (FFCA) and finally formed FDCA. The chronoamperometry electrolysis measurements of HMFOR on NiCo-Pi-LDHs/NF were performed at 1.425 V vs. RHE in a H-type electrochemical cell using Fumasep FAA-3-PK-130 as an anion exchange membrane. High-performance liquid chromatography (HPLC) was used to monitor and quantify the conversion of HMF and the yield of oxidation products (Figure S13). Since it took six electrons to oxidize one HMF molecule into one FDCA molecule, a theoretical charge of 86.7 C was required for completely converting 1.5×10^{-4} mole of HMF into FDCA. During the electrolysis, the electrolyte color changed from initial yellow to almost colorless, indicating the oxidation of HMF. As shown in Fig. 4B, HMF was gradually consumed in the electrooxidation process, accompanied by the generation of FDCA. In addition, HMFCA was also detected in the HMFOR process, while DFF was not found. This manifested that the reaction pathway was the preferred oxidation of aldehyde groups in HMF to generate HMFCA, consistent with previous literature [55–57]. The HMFCA was then oxidized into FFCA and finally, FDCA. Meanwhile, FFCA was not detected, manifesting the transformation from FFCA into FDCA was rapid, and the activation of HMFCA was the rate-controlling step of the reaction. After consuming 86.7 C of charge, HMF totally oxidized into FDCA with a high faradaic efficiency (FE) of 99.6 %. To explore the selectivity and FE of FDCA under different applied potentials, HMF electrooxidations were also conducted under potentials of 1.375, 1.425, 1.475, and 1.525 V vs. RHE, respectively. As shown in Fig. 4C, the NiCo-Pi-LDHs/NF exhibited high oxidation efficiency in a wide potential window from 1.375 to 1.475 vs. RHE with the FE of FDCA above 96 %. Higher FDCA selectivity and FE were achieved at lower potentials (1.375 and 1.425 V vs. RHE). As the potential was further raised to 1.475 and 1.525 V vs. RHE, the selectivity, and FE of FDCA gradually decreased, resulting from competitive OER. The above results clearly demonstrated that the optimal potential for HMF electrooxidation to FDCA over NiCo-Pi-LDHs/NF electrode was 1.425 V. The durability of catalyst is one of the most important indexes for catalytic performance and was assessed by successive HMF oxidation and long-term OER. For HMF oxidation, five successive electrolysis at a potential of 1.425 V vs. RHE under 10 mmol HMF with the same electrode were conducted. The HMF conversion (99.3 %~100 %) as well as the selectivity (99.3 %–99.8 %) and FE (98.8 %–99.6 %) of FDCA fluctuate in narrow ranges (Fig. 4D). Moreover, as shown in Figure S14, five successive electrolysis at a potential of 1.425 V vs. RHE under 50 mmol HMF were also conducted. The HMF conversion (98.8 %~99.3 %) as well as the selectivity (99.0 %~99.6 %) and FE (97.7 %~98.9 %) of FDCA were achieved. As displayed in Table S6, there was no significant difference in the P content of the NiCo-Pi-LDHs catalyst before and after 5 cycles of electrolysis, suggesting that the intercalated phosphate
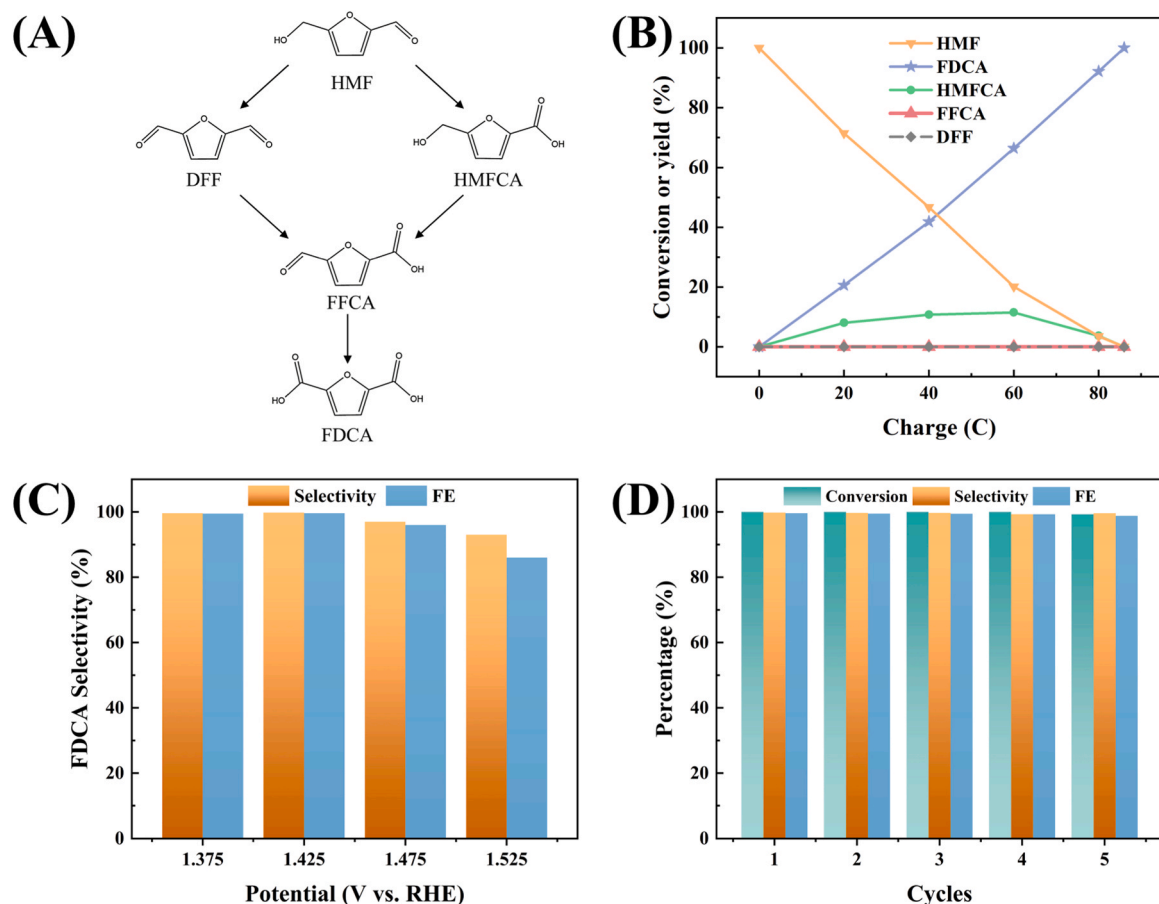
Fig. 4. (A) Two possible reaction pathways of HMF oxidation into FDCA. (B) The conversion of HMF and the yield of different oxidation products during HMFOR. (C) The selectivity of FDCA and FE at different potentials. (D) The HMF conversion, FDCA selectivity, and FE obtained by NiCo-Pi-LDHs/NF for five consecutive cycles of HMFOR.

anions were stable. Additionally, the morphology of NiCo-Pi-LDHs/NF after 5-cycles electrolysis was also characterized. As displayed in Figure S15, NiCo-Pi-LDHs nanosheets remained tightly attached to the nickel foam framework without any noticeable exfoliation, illustrating the good durability of the catalysts. For long-term OER, Figure S16 showed that the initial current density (55.4 mA/cm^2) decreased by only 1.8 mA/cm^2 after 10 h in 1.0 M KOH, confirming the good electrochemical stability of NiCo-Pi-LDHs/NF. The above results indicated that the NiCo-Pi-LDHs/NF was an efficient and robust electrocatalyst for

HMFOR.

3.4. Reaction mechanism over NiCo-Pi-LDHs/NF catalyst

To investigate the effect of phosphate intercalation on the electronic environment, XPS was conducted over catalysts. Fig. 5A and Fig. 5B exhibited the Ni 2p spectra and Co 2p spectra, with the deconvolution of the Gaussian peak fitting method of the samples. As shown in Fig. 5A, the Ni 2p spectrum of NiCo-Ci-LDHs can be fitted with two spin-orbit
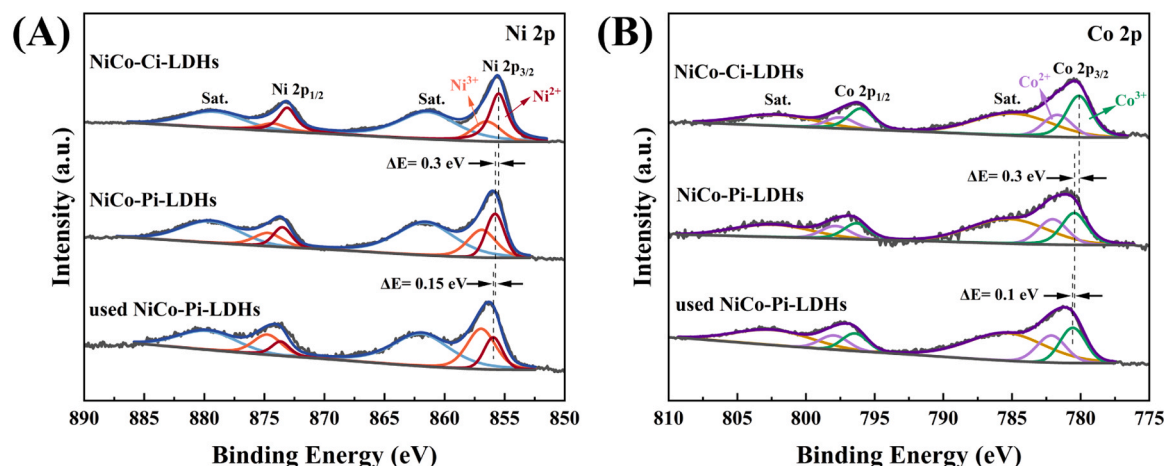

Fig. 5. XPS spectra of Ni 2p (A) and Co 2p (B) for NiCo-Ci-LDHs, NiCo-Pi-LDHs, and the used NiCo-Pi-LDHs.

doublet peaks, including the binding energies at 855.5 eV (Ni 2p$_{3/2}$) and 873.2 eV (Ni 2p$_{1/2}$) for Ni^{2+}, 856.5 eV (Ni 2p$_{3/2}$) and 874.2 eV (Ni 2p$_{1/2}$) for Ni^{3+}, respectively. Compared with those of NiCo-Ci-LDHs, shifts of Ni species (0.3 eV) towards high binding energy in NiCo-Pi-LDHs were observed, which implied the intercalation of phosphate anion modulated the electronic structure of Ni center. More importantly, as shown in Table 2, compared to that of NiCo-Ci-LDHs, the Ni^{3+}/Ni^{2+} ratio was increased from 0.46 to 1.08 in NiCo-Pi-LDHs, indicating the intercalation of phosphate contributed to the evocation of high valence Ni species. In the meantime, shifts of Co species towards high binding energy and the decrease of Co^{3+}/Co^{2+} ratio from 1.86 to 1.25 in NiCo-Pi-LDHs were also observed. Such electronic environment changes can be attributed to the intercalation of phosphate anion, which boosted partial charge transfer from Ni to Co sites [32]. After HMF electrooxidation, the Ni 2p peaks shifted ~0.15 eV to higher binding energies, and Ni^{3+}/Ni^{2+} further increased to 2.03. Correspondingly, the binding energy of Co raised 0.1 eV, accompanied by a slight decrease of the Co^{3+}/Co^{2+} ratio to 1.10. Apparently, since the change of Co species electronic environment was relatively weak, the significant change of Ni species electronic environment in NiCo-Pi-LDHs before and after HMFOR cannot be solely attributed to the charge transfer between Ni and Co. Therefore, the in situ evolution of the intercalated phosphate anion during HMF electrooxidation may be the main reason for the optimization of electronic structure and the evocation of high valence Ni species.

In order to demonstrate the evolution of intercalated phosphate anions during HMFOR, FTIR of used NiCo-Pi-LDHs was conducted to confirm the transformation of intercalated phosphate anion. As shown in Fig. 6A, the features detected at 1109 cm^{-1} and 1061 cm^{-1} were attributed to the antisymmetric stretching vibration of O-P=O and stretching vibration of P-O, respectively [58]. More importantly, the characteristic peak at 1021 cm^{-1} was assigned to the stretching vibration of the P-OH bond, manifesting the simultaneous existence of HPO$_4^{2-}$ in the used NiCo-Pi-LDHs [59]. Moreover, the peak at 854 cm^{-1} was assigned to the M-O vibration mode of NiCo-LDH, demonstrating that the in situ evolution of the intercalated phosphate anion did not affect the layered structure of metallic hydroxides. Meanwhile, the XPS spectra of P 2p of NiCo-Pi-LDHs before and after HMFOR were analyzed. As shown in Fig. 6B, the P 2p XPS spectrum showed that the NiCo-Pi-LDHs before HMFOR exhibited characteristic peaks at 132.7 eV, corresponding to phosphate anion. The peak shifted to a higher binding energy (133.1 eV) in the NiCo-Pi-LDHs after HMFOR, but it is lower than the HPO$_4^{2-}$ anion [60]. The above results revealed the tendency for the intercalated PO$_4^{3-}$ to evolve into HPO$_4^{2-}$ during the HMF electrooxidation and the co-existence of two anions after reaction. Another important issue was whether the formed HPO$_4^{2-}$ can be converted back into PO$_4^{3-}$ anion. Theoretically, the HPO$_4^{2-}$ was easily converted to PO$_4^{3-}$ in basic solution, especially under the applied anodic potential [61–63]. To confirm the conversion, sodium phosphate dibasic was used to synthesize HPO$_4^{2-}$ intercalated NiCo-LDHs (NiCo-HPi-LDHs), further immersed in 1.0 M KOH electrolyte. As depicted in Figure S17, the XRD pattern of NiCo-HPi-LDHs treated in basic electrolyte exhibited the typical characteristic reflections of LDHs materials. Meanwhile, the (003) diffraction peak occurred at 2θ=8.7°, corresponding to the intercalation of PO$_4^{3-}$ rather than HPO$_4^{2-}$ [59]. This result strongly suggested that the HPO$_4^{2-}$ anions presented in the NiCo-LDHs interlayer can be converted back to PO$_4^{3-}$ under alkaline conditions.

In situ electrochemical impedance spectroscopy (EIS) was used to establish the relationship between interfacial kinetics and charge

transfer during HMF electrooxidation at different potentials. As illustrated in Fig. 6C and Fig. 6D, the low frequency region (10^{-1}~10^1 Hz) was associated with the non-uniform charge distribution induced by the HMFOR, namely the oxidation behavior occurring at the interface between the electrode and electrolyte. The high frequency region (10^1~10^5 Hz) was associated with oxidation within the electrode [53,64]. In Fig. 6C, for NiCo-Pi-LDHs/NF, it was observed that the phase angle in high frequency region dramatically decreased with the increase of potential in the interval of 1.05–1.25 V vs. RHE and finally remained constant at 1.35 V vs. RHE. In contrast, as shown in Fig. 6D, the phase angle in high frequency region slowly decreased from 1.05 to 1.55 V vs. RHE, suggesting the electrochemical oxidation within the NiCo-Ci-LDHs/NF was more sluggish than NiCo-Pi-LDHs/NF. Meanwhile, it was observed that the phase angle values of NiCo-Pi-LDHs/NF in the low frequency region were significantly lower than those of NiCo-Ci-LDHs/NF, indicating the accelerated reaction kinetics of the NiCo-Pi-LDHs electrocatalyst. As illustrated in Fig. 6E, the intercalated phosphate anion enhanced Ni(OH)$_2$/NiOOH transformation by promoting the interlayer dehydrogenation process. More delightfully, in combination with the results of electrochemical measurement, it can be concluded that the boosted Ni(OH)$_2$/NiOOH transformation was beneficial for increasing the active sites, promoting the intrinsic activity and thereby enhancing the current density of HMFOR.

DFT calculations were performed on NiCo-Pi-LDHs and NiCo-Pi-LDHs to further reveal the influence of phosphate intercalation on HMF electrooxidation. The density of states (DOS) of NiCo-Pi-LDHs and NiCo-Ci-LDHs were displayed in Fig. 7A and Fig. 7B, respectively. Compared to NiCo-Ci-LDHs, NiCo-Pi-LDHs showed a higher total density of states surrounding the Femi level, indicating a promoted electrical conductivity, demonstrating the contribution of intercalated phosphate anions on electron transfer. The Bader charge analysis was further performed to verify the effect of phosphate intercalation on the electron density of metal sites. As shown in Fig. 7C, the Bader electrons of nickel atoms in NiCo-Ci-LDHs was calculated to be +8.77 e$^-$. For NiCo-Pi-LDHs, the valence electrons were transferred from the nickel sites to neighboring cobalt sites, and the Bader electrons for the neighboring nickel sites was 8.71 e$^-$. Meanwhile, Bader electrons of Co was increased from 7.61 e$^-$ to 7.66 e$^-$. This result revealed that phosphate intercalation facilitated the electron transfer from Ni to Co, inducing the generation of Ni^{3+} species, which was owing to the strong electron coupling between the metal sites and phosphate anion [65].

Based on the above analysis, the superior HMFOR performance of the NiCo-Pi-LDHs catalyst was ascribed to the high-valence nickel species induced by the intercalation of phosphate anions. Firstly, introducing phosphate anions facilitated the electron transfer from Ni to Co, which contributed to the evocation of high valence Ni species. Secondly, the strong nucleophilic phosphate anion acted as a proton transfer intermediate to promote the dehydrogenation step of hydroxides to form (oxy)hydroxide, thereby increasing the proportion of high-valence nickel species. The dehydrogenation process occurring in the interlayer was particularly favorable for generating high-valence nickel species in the bulk phase, which significantly improved electron transport and reduced charge transfer resistance. On the basis of the above evidence and previous reports in literatures, a dual-cycle mechanism can be drawn, as shown in Fig. 7D. In simply terms, the intercalated phosphate anions acted as proton transfer mediators for the dehydrogenation of Ni(OH)$_2$ and promoted the formation of NiOOH while transforming itself into HPO$_4^{2-}$. Subsequently, the generated NiOOH chemically oxidized HMF into FDCA and itself reduced backward to Ni(OH)$_2$. Simultaneously, HPO$_4^{2-}$ reacted with the hydroxyl group in the electrolyte and rapidly oxidized back to PO$_4^{3-}$. The resulting dual-cycle mechanism facilitated the formation of high-valence nickel species and, therefore, remarkably enhanced the catalytic performance in HMF electrooxidation.

Table 2
The ratio of Ni^{3+}/Ni^{2+} and Co^{3+}/Co^{2+} obtained from XPS results.

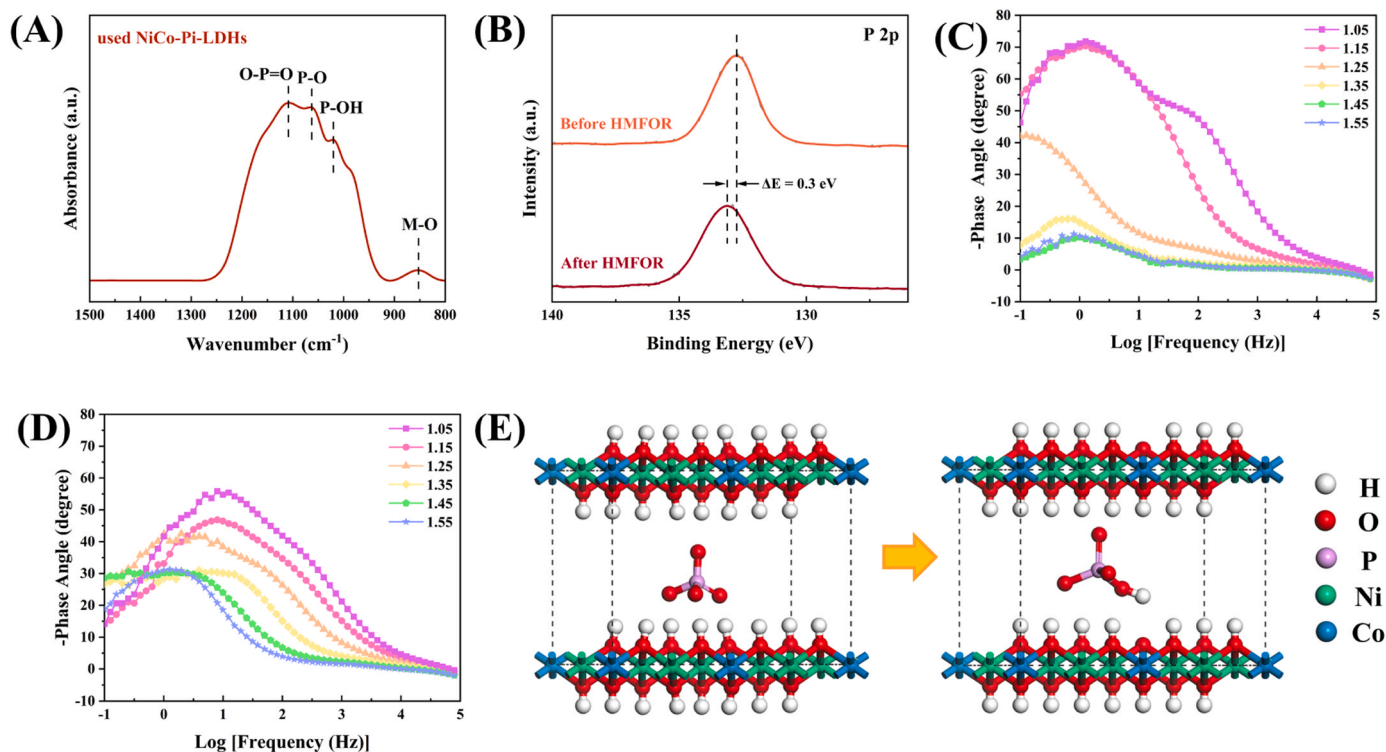| Samples	Ni^{3+}/Ni^{2+}	Co^{3+}/Co^{2+}
NiCo-Ci-LDHs	0.46	1.86
NiCo-Pi-LDHs	1.08	1.25
Used NiCo-Pi-LDHs	2.03	1.10

Fig. 6. (A) FTIR spectrum of used NiCo-Pi-LDHs. (B) XPS spectra of P 2p for NiCo-Pi-LDHs before and after HMFOR. (C) Bode phase plot for NiCo-Pi-LDHs/NF. (D) Bode phase plot for NiCo-Ci-LDHs/NF. (E) The scheme of phosphate encouraging the dehydrogenation of laminate.
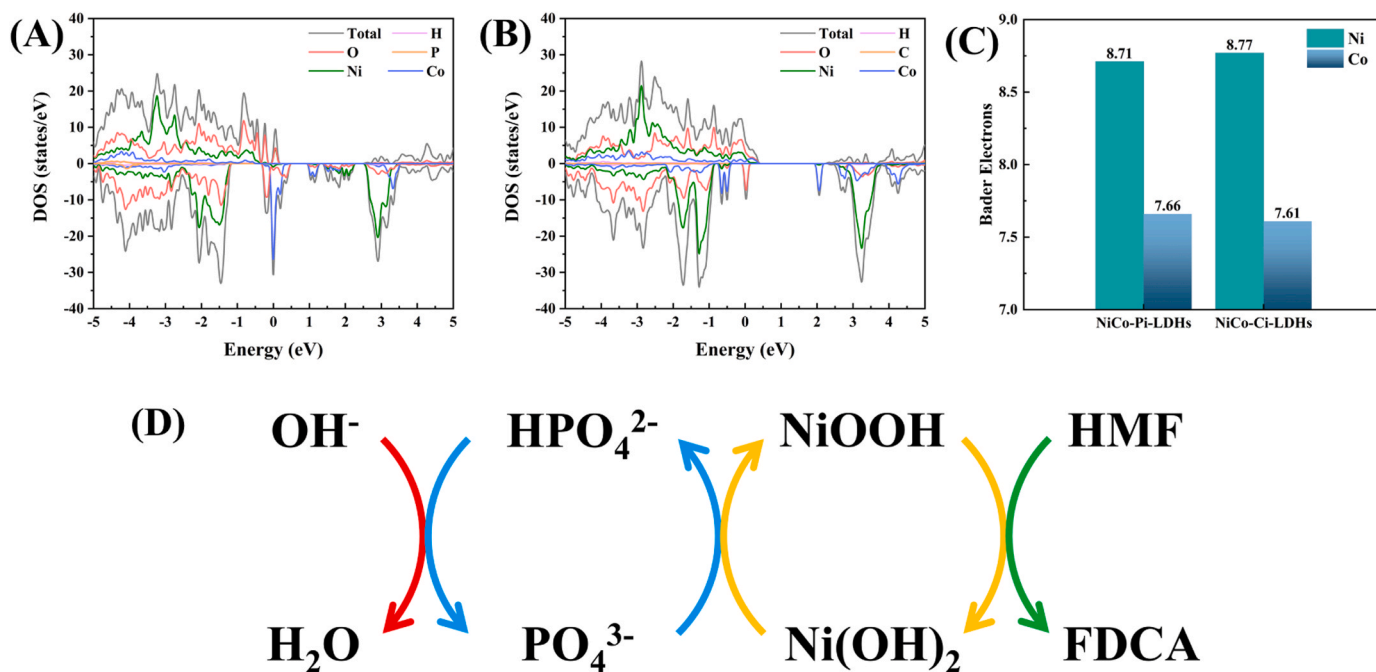

Fig. 7. (A) Total density of states (TDOS) curves of NiCo-Pi-LDHs. (B) Total density of states (TDOS) curves of NiCo-Ci-LDHs. (C) Bader electrons for Ni and Co in NiCo-Pi-LDHs and NiCo-Ci-LDHs. (D) The possible reaction mechanism over NiCo-Pi-LDHs catalysts.

4. Conclusion

In this work, phosphate anion intercalated NiCo-Pi-LDHs catalyst was synthesized via the anion exchange method by using NiCo-LDHs as a precursor. The structure of the NiCo-Pi-LDHs catalyst was identified by a series of experiments and DFT calculation. The intercalated phosphate anion promoted the electron transfer from Ni to Co, and facilitated the dehydrogenation process of NiCo-LDHs as a proton transfer intermediate. Furthermore, it boosted the generation of high-valence nickel species via the protonation cycle, thus improved the hydroxides/oxyhydroxides transformation cycle, increasing the number of active sites and promoting intrinsic activity. Benefiting from the dual-circle

mechanism, the NiCo-Pi-LDHs exhibited competitive electrocatalytic performance for HMFOR with a low onset potential of 1.16 V vs. RHE and a current density of 200 mA/cm^2 at only 1.41 V vs. RHE. The NiCo-Pi-LDHs displayed selectivity and Faradic efficiency of FDCA nearly 100 %, and robust stability for 5 cycles. In summary, this work provided a new idea to boost the generation of high-valence nickel sites for HMFOR, which also drew some reference to other organic electrochemical oxidations.

CRediT authorship contribution statement

Tianli Hui: Writing – original draft, Methodology, Investigation, Data curation. **Haowei Liu:** Methodology, Investigation. **Tonghui Li:** Methodology, Investigation. **Jinbo Pan:** Writing – review & editing, Methodology, Investigation. **Tao Zheng:** Writing – review & editing, Supervision, Conceptualization. **Rui Zhang:** Supervision, Methodology, Investigation. **Xianghai Meng:** Writing – review & editing, Supervision, Conceptualization. **Haiyan Liu:** Writing – review & editing, Supervision, Conceptualization. **Zhichang Liu:** Writing – review & editing, Supervision, Conceptualization. **Chunming Xu:** Supervision, Resources, Conceptualization.

Declaration of Competing Interest

The authors declare that they have no known competing financial interests or personal relationships that could have appeared to influence the work reported in this paper.

Data availability

Data will be made available on request.

Acknowledgment

Appendix A. Supporting information

Supplementary data associated with this article can be found in the online version at doi:10.1016/j.apcatb.2024.124147.

References

[1] Y. Zhang, Y. Shen, Electrochemical hydrogenation of levulinic acid, furfural and 5-hydroxymethylfurfural, Appl. Catal. B: Environ. 343 (2024) 123576.

[2] L. Gao, Z. Liu, J. Ma, L. Zhong, Z. Song, J. Xu, S. Gan, D. Han, L. Niu, NiSe@NiOx core-shell nanowires as a non-precious electrocatalyst for upgrading 5-hydroxymethylfurfural into 2,5-furandicarboxylic acid, Appl. Catal. B: Environ. 261 (2020) 118235.

[3] W. Ma, G. Liu, Q. Wang, J. Liu, X. Yuan, J. Xin, S. Wang, H. He, Ionic liquids enhance the electrocatalysis of lignin model compounds towards generating valuable aromatic molecules, J. Mol. Liq. 367 (2022) 120407.

[4] G. Liu, Q. Wang, D. Yan, Y. Zhang, C. Wang, S. Liang, L. Jiang, H. He, Insights into the electrochemical degradation of phenolic lignin model compounds in a protic ionic liquid-water system, Green. Chem. 23 (2021) 1665–1677.

[5] Y. Zhu, W. Zhao, J. Zhang, Z. An, X. Ma, Z. Zhang, Y. Jiang, L. Zheng, X. Shu, H. Song, X. Xiang, J. He, Selective activation of C-OH, C-O-C, or C=C in furfuryl alcohol by engineered Pt sites supported on layered double oxides, ACS Catal. 10 (2020) 8032–8041.

[6] C. Xu, E. Paone, D. Rodriguez-Padron, R. Luque, F. Mauriello, Recent catalytic routes for the preparation and the upgrading of biomass derived furfural and 5-hydroxymethylfurfural, Chem. Soc. Rev. 49 (2020) 4273–4306.

[7] S. Li, X. Sun, Z. Yao, X. Zhong, Y. Cao, Y. Liang, Z. Wei, S. Deng, G. Zhuang, X. Li, J. Wang, Biomass valorization via paired electrosynthesis over vanadium nitride-based electrocatalysts, Adv. Funct. Mater. 29 (2019) 1904780.

[8] M. Sajid, X. Zhao, D. Liu, Production of 2,5-furandicarboxylic acid (FDCA) from 5-hydroxymethylfurfural (HMF): recent progress focusing on the chemical-catalytic routes, Green. Chem. 20 (2018) 5427–5453.

[9] D.A. Giannakoudakis, J.C. Colmenares, D. Tsiplakides, K.S. Triantafyllidis, Nanoengineered electrodes for biomass-derived 5-hydroxymethylfurfural electrocatalytic oxidation to 2,5-furandicarboxylic acid, ACS Sustain. Chem. Eng. 9 (2021) 1970–1993.

[10] I. Mondal, P.V. Menezes, K. Laun, T. Diemant, M. Al-Shakran, I. Zebger, T. Jacob, M. Driess, P.W. Menezes, In-liquid plasma-mediated manganese oxide electrocatalysts for quasi-industrial water oxidation and selective dehydrogenation, ACS Nano 17 (2023) 14043–14052.

[11] J.N. Hausmann, P.V. Menezes, G. Vijaykumar, K. Laun, T. Diemant, I. Zebger, T. Jacob, M. Driess, P.W. Menezes, In-liquid plasma modified nickel foam: NiOOH/NiFeOOH active site multiplication for electrocatalytic alcohol, aldehyde, and water oxidation, Adv. Energy Mater. 12 (2022) 2202098.

[12] Z.-Y. Yu, Y. Duan, X.-Y. Feng, X. Yu, M.-R. Gao, S.-H. Yu, Clean and affordable hydrogen fuel from alkaline water splitting: past, recent progress, and future prospects, Adv. Mater. 33 (2021) 2007100.

[13] H.-Y. Wang, M.-L. Sun, J.-T. Ren, Z.-Y. Yuan, Circumventing challenges: design of anodic electrocatalysts for hybrid water electrolysis systems, Adv. Energy Mater. 13 (2023) 2203568.

[14] D. Chen, Y. Ding, X. Cao, L. Wang, H. Lee, G. Lin, W. Li, G. Ding, L. Sun, Highly efficient biomass upgrading by a Ni-Cu electrocatalyst featuring passivation of water oxidation activity, Angew. Chem. Int. Ed. 62 (2023) e202309478.

[15] J. Zhang, W. Gong, H. Yin, D. Wang, Y. Zhang, H. Zhang, G. Wang, H. Zhao, Situ growth of ultrathin Ni(OH)2 nanosheets as catalyst for electrocatalytic oxidation reactions, ChemSusChem 14 (2021) 2935–2942.

[16] B.J. Taitt, D.-H. Nam, K.-S. Choi, A comparative study of nickel, cobalt, and iron oxyhydroxide anodes for the electrochemical oxidation of 5-hydroxymethylfurfural to 2,5-furandicarboxylic acid, ACS Catal. 9 (2019) 660–670.

[17] Z. Yang, B. Zhang, C. Yan, Z. Xue, T. Mu, The pivot to achieve high current density for biomass electrooxidation: accelerating the reduction of Ni3+ to Ni2+, Appl. Catal. B: Environ. 330 (2023) 122590.

[18] B. Zhang, H. Fu, T. Mu, Hierarchical NiSx/Ni2P nanotube arrays with abundant interfaces for efficient electrocatalytic oxidation of 5-hydroxymethylfurfural, Green. Chem. 24 (2022) 877–884.

[19] M. Cai, Y. Zhang, Y. Zhao, Q. Liu, Y. Li, G. Li, Two-dimensional metal-organic framework nanosheets for highly efficient electrocatalytic biomass 5-(hydroxymethyl)furfural (HMF) valorization, J. Mater. Chem. A 8 (2020) 20386–20392.

[20] M. Guo, X. Lu, J. Xiong, R. Zhang, X. Li, Y. Qiao, N. Ji, Z. Yu, Alloy-driven efficient electrocatalytic oxidation of biomass-derived 5-hydroxymethylfurfural towards 2,5-furandicarboxylic acid: a review, ChemSusChem 15 (2022) e202201074.

[21] B. Liu, S. Xu, M. Zhang, X. Li, D. Decarolis, Y. Liu, Y. Wang, E.K. Gibson, C.R. A. Catlow, K. Yan, Electrochemical upgrading of biomass-derived 5-hydroxymethylfurfural and furfural over oxygen vacancy-rich NiCoMn-layered double hydroxides nanosheets, Green. Chem. 23 (2021) 4034–4043.

[22] X. Deng, X. Kang, M. Li, K. Xiang, C. Wang, Z. Guo, J. Zhang, X.-Z. Fu, J.-L. Luo, Coupling efficient biomass upgrading with H2 production via bifunctional CuxS@NiCo-LDH core-shell nanoarray electrocatalysts, J. Mater. Chem. A 8 (2020) 1138–1146.

[23] R. Luo, Y. Li, L. Xing, N. Wang, R. Zhong, Z. Qian, C. Du, G. Yin, Y. Wang, L. Du, A dynamic Ni(OH)2-NiOOH/NiFeP heterojunction enabling high-performance E-upgrading of hydroxymethylfurfural, Appl. Catal. B: Environ. (2022) 121357.

[24] J. Kang, X. Qiu, Q. Hu, J. Zhong, X. Gao, R. Huang, C. Wan, L.-M. Liu, X. Duan, L. Guo, Valence oscillation and dynamic active sites in monolayer NiCo hydroxides for water oxidation, Nat. Catal. 4 (2021) 1050–1058.

[25] Y. Hao, J. Li, X. Cao, L. Meng, J. Wu, X. Yang, Y. Li, Z. Liu, M. Gong, Origin of the universal potential-dependent organic oxidation on nickel oxyhydroxide, ACS Catal. 13 (2023) 2916–2927.

[26] C. Yang, C. Laberty-Robert, D. Batuk, G. Cibin, A.V. Chadwick, V. Pimenta, W. Yin, L. Zhang, J.-M. Tarascon, A. Grimaud, Phosphate ion functionalization of perovskite surfaces for enhanced oxygen evolution reaction, J. Phys. Chem. Lett. 8 (2017) 3466–3472.

[27] Q. Yin, D. Rao, G. Zhang, Y. Zhao, J. Han, K. Lin, L. Zheng, J. Zhang, J. Zhou, M. Wei, CoFe-Cl layered double hydroxide: a new cathode material for high-performance chloride ion batteries, Adv. Funct. Mater. 29 (2019) 1900983.

[28] L. Dang, H. Liang, J. Zhuo, B.K. Lamb, H. Sheng, Y. Yang, S. Jin, Direct synthesis and anion exchange of noncarbonate-intercalated NiFe-layered double hydroxides and the influence on electrocatalysis, Chem. Mater. 30 (2018) 4321–4330.

[29] J.Y.C. Chen, L. Dang, H. Liang, W. Bi, J.B. Gerken, S. Jin, E.E. Alp, S.S. Stahl, Operando analysis of NiFe- and Fe-oxyhydroxide electrocatalysts for water oxidation: detection of Fe4+ by Mossbauer spectroscopy, J. Am. Chem. Soc. 137 (2015) 15090–15093.

[30] H.-M. Liu, X.-J. Zhao, Y.-Q. Zhu, H. Yan, DFT study on MgAl-layered double hydroxides with different interlayer anions: structure, anion exchange, host-guest interaction and basic sites, Phys. Chem. Chem. Phys. 22 (2020) 2521–2529.

[31] X.-J. Zhao, Y.-Q. Zhu, S.-M. Xu, H.-M. Liu, P. Yin, Y.-L. Feng, H. Yan, Anion exchange behavior of MIIIAl layered double hydroxides: a molecular dynamics and DFT study, Phys. Chem. Chem. Phys. 22 (2020) 19758–19768.

[32] M. Luo, Z. Cai, C. Wang, Y. Bi, L. Qian, Y. Hao, L. Li, Y. Kuang, Y. Li, X. Lei, Z. Huo, W. Liu, H. Wang, X. Sun, X. Duan, Phosphorus oxoanion-intercalated layered double hydroxides for high-performance oxygen evolution, Nano Res. 10 (2017) 1732–1739.

[33] B. Zhang, S. Liu, S. Zhang, Y. Cao, H. Wang, C. Han, J. Sun, High corrosion resistance of NiFe-layered double hydroxide catalyst for stable seawater electrolysis promoted by phosphate intercalation, Small 18 (2022) 2203852.

[34] C. Guo, W. Zhou, X. Lan, Y. Wang, T. Li, S. Han, Y. Yu, B. Zhang, Electrochemical upgrading of formic acid to formamide via coupling nitrite co-reduction, J. Am. Chem. Soc. (2022).

[35] M. Gao, J. Fan, X. Li, Q. Wang, D. Li, J. Feng, X. Duan, A carbon-negative hydrogen production strategy: CO2 selective capture with H2 production, Angew. Chem. Int. Ed. 62 (2023) e202216527.

[36] C. Miao, T. Hui, Y. Liu, J. Feng, D. Li, Pd/MgAl-LDH nanocatalyst with vacancy-rich sandwich structure: Insight into interfacial effect for selective hydrogenation, J. Catal. 370 (2019) 107–117.

[37] Y. Wang, Q. Pan, Y. Qiao, X. Wang, D. Deng, F. Zheng, B. Chen, J. Qiu, Layered metal oxide nanosheets with enhanced interlayer space for electrochemical deionization, Adv. Mater. 35 (2023) 2210871.

[38] T. Guo, L. Chen, Y. Li, K. Shen, Controllable synthesis of ultrathin defect-rich LDH nanoarrays coupled with MOF-derived Co-NC microarrays for efficient overall water splitting, Small 18 (2022) 2107739.

[39] X. Wang, H. Huang, J. Qian, Y. Li, K. Shen, Intensified Kirkendall effect assisted construction of double-shell hollow Cu-doped CoP nanoparticles anchored by carbon arrays for water splitting, Appl. Catal. B: Environ. 325 (2023) 122295.

[40] S. Xie, H. Fu, L. Chen, Y. Li, K. Shen, Carbon-based nanoarrays embedded with Ce-doped ultrasmall Co2P nanoparticles enable efficient electrooxidation of 5-hydroxymethylfurfural coupled with hydrogen production, Sci. China Chem. 66 (2023) 2141–2152.

[41] Z. Yuan, H. Wang, J. Shen, P. Ye, J. Ning, Y. Zhong, Y. Hu, Hierarchical Cu2S@NiCo-LDH double-shelled nanotube arrays with enhanced electrochemical performance for hybrid supercapacitors, J. Mater. Chem. A 8 (2020) 22163–22174.

[42] J. Liu, H. Tang, P. Jian, B. Liu, Oxygen-vacancy defect engineering to boost the aerobic oxidation of limonene over Co3O4 nanocubes, Appl. Catal. B: Environ. 334 (2023) 122828.

[43] J. Liu, H. Wang, L. Wang, P. Jian, X. Yan, Phase-dependent catalytic performance of MnO2 for solvent-free oxidation of ethybenzene with molecular oxygen, Appl. Catal. B: Environ. 305 (2022) 121050.

[44] N.K. Chaudhari, H. Jin, B. Kim, K. Lee, Nanostructured materials on 3D nickel foam as electrocatalysts for water splitting, Nanoscale 9 (2017) 12231–12247.

[45] A. Goswami, D. Ghosh, D. Pradhan, K. Biradha, In situ grown Mn(II) MOF upon nickel foam acts as a robust self-supporting bifunctional electrode for overall water splitting: a bimetallic synergistic collaboration strategy, ACS Appl. Mater. Interfaces 14 (2022) 29722–29734.

[46] J.J. Roylance, T.W. Kim, K.-S. Choi, Efficient and selective electrochemical and photoelectrochemical reduction of 5-hydroxymethylfurfural to 2,5-bis(hydroxy-methyl)furan using water as the hydrogen source, ACS Catal. 6 (2016) 1840–1847.

[47] W.-J. Liu, L. Dang, Z. Xu, H.-Q. Yu, S. Jin, G.W. Huber, Electrochemical oxidation of 5-hydroxymethylfurfural with NiFe layered double hydroxide (LDH) nanosheet catalysts, ACS Catal. 8 (2018) 5533–5541.

[48] T. Wu, Z. Xu, X. Wang, M. Luo, Y. Xia, X. Zhang, J. Li, J. Liu, J. Wang, H.-L. Wang, F. Huang, Surface-confined self-reconstruction to sulfate-terminated ultrathin layers on NiMo3S4 toward biomass molecule electro-oxidation, Appl. Catal. B: Environ. 323 (2023) 122126.

[49] J.N. Hausmann, R. Beltran-Suito, S. Mebs, V. Hlukhyy, T.F. Fassler, H. Dau, M. Driess, P.W. Menezes, Evolving highly active oxidic iron(III) phase from corrosion of intermetallic iron silicide to master efficient electrocatalytic water oxidation and selective oxygenation of 5-hydroxymethylfurfural, Adv. Mater. 33 (2021) 2008823.

[50] Y. Song, Z. Li, K. Fan, Z. Ren, W. Xie, Y. Yang, M. Shao, M. Wei, Ultrathin layered double hydroxides nanosheets array towards efficient electrooxidation of 5-hydroxymethylfurfural coupled with hydrogen generation, Appl. Catal. B: Environ. 299 (2021) 120669.

[51] Y. Xie, Z. Zhou, N. Yang, G. Zhao, An overall reaction integrated with highly selective oxidation of 5-hydroxymethylfurfural and efficient hydrogen evolution, Adv. Funct. Mater. 31 (2021) 2102886.

[52] Y. Feng, K. Yang, R.L. Smith, X. Qi, Metal sulfide enhanced metal-organic framework nanoarrays for electrocatalytic oxidation of 5-hydroxymethylfurfural to 2,5-furandicarboxylic acid, J. Mater. Chem. A 11 (2023) 6375–6383.

[53] S. Li, S. Wang, Y. Wang, J. He, K. Li, Y. Xu, M. Wang, S. Zhao, X. Li, X. Zhong, J. Wang, Doped Mn enhanced NiS electrooxidation performance of HMF into FDCA at industrial-level current density, Adv. Funct. Mater. 33 (2023) 2214488.

[54] X. Deng, M. Li, Y. Fan, L. Wang, X.-Z. Fu, J.-L. Luo, Constructing multifunctional 'Nanoplatelet-on-Nanoarray' electrocatalyst with unprecedented activity towards novel selective organic oxidation reactions to boost hydrogen production, Appl. Catal. B: Environ. 278 (2020) 119339.

[55] M.T. Bender, X. Yuan, M.K. Goetz, K.-S. Choi, Electrochemical hydrogenation, hydrogenolysis, and dehydrogenation for reductive and oxidative biomass upgrading using 5-hydroxymethylfurfural as a model system, ACS Catal. 12 (2022) 12349–12368.

[56] H. Yang, P.V. Menezes, G. Dai, G. Vijaykumar, Z. Chen, M. Al-Shakran, T. Jacob, M. Driess, P.W. Menezes, Activation of nickel foam through in-liquid plasma-induced phosphorus incorporation for efficient quasi-industrial water oxidation and selective oxygenation of organics, Appl. Catal. B: Environ. 324 (2023) 122249.

[57] Y. Song, W. Xie, Y. Song, H. Li, S. Li, S. Jiang, J.Y. Lee, M. Shao, Bifunctional integrated electrode for high-efficient hydrogen production coupled with 5-hydroxymethylfurfural oxidation, Appl. Catal. B: Environ. 312 (2022) 121400.

[58] X. Xu, X. Song, X. Liu, H. Wang, Y. Hu, J. Xia, J. Chen, M. Shakouri, Y. Guo, Y. Wang, A highly efficient nickel phosphate electrocatalyst for the oxidation of 5-hydroxymethylfurfural to 2,5-furandicarboxylic acid, ACS Sustain. Chem. Eng. 10 (2022) 5538–5547.

[59] Y. Guo, J. Wang, D. Li, P. Tang, F. Leroux, Y. Feng, Micrometer-sized dihydrogenphosphate-intercalated layered double hydroxides: synthesis, selective infrared absorption properties, and applications as agricultural films, Dalton Trans. 47 (2018) 3144–3154.

[60] P.H. Lo, W.T. Tsai, J.T. Lee, M.P. Hung, The electrochemical behavior of electroless plated Ni-P alloys in concentrated NaOH solution, J. Electrochem. Soc. 142 (1995) 91.

[61] D. Zhou, Z. Cai, Y. Bi, W. Tian, M. Luo, Q. Zhang, Q. Zhang, Q. Xie, J. Wang, Y. Li, Y. Kuang, X. Duan, M. Bajdich, S. Siahrostami, X. Sun, Effects of redox-active interlayer anions on the oxygen evolution reactivity of NiFe-layered double hydroxide nanosheets, Nano Res. 11 (2018) 1358–1368.

[62] Y. Li, R. Tong, W. Zhang, S. Peng, Pre-intercalation of phosphate into Ni(OH)2/NiOOH for efficient and stable electrocatalytic oxygen evolution reaction, J. Catal. 410 (2022) 22–30.

[63] D.-H. Nam, K.-S. Choi, Electrochemical Bi/BiPO4 cells for a sustainable phosphate cycle, ACS Energy Lett. 8 (2023) 802–808.

[64] G. Zhao, G. Hai, P. Zhou, Z. Liu, Y. Zhang, B. Peng, W. Xia, X. Huang, G. Wang, Electrochemical oxidation of 5-hydroxymethylfurfural on CeO2-modified Co3O4 with regulated intermediate adsorption and promoted charge transfer, Adv. Funct. Mater. 33 (2023) 2213170.

[65] S. Zhou, J. Wang, J. Li, L. Fan, Z. Liu, J. Shi, W. Cai, Surface-growing organophosphorus layer on layered double hydroxides enables boosted and durable electrochemical freshwater/seawater oxidation, Appl. Catal. B: Environ. (2023) 122749.